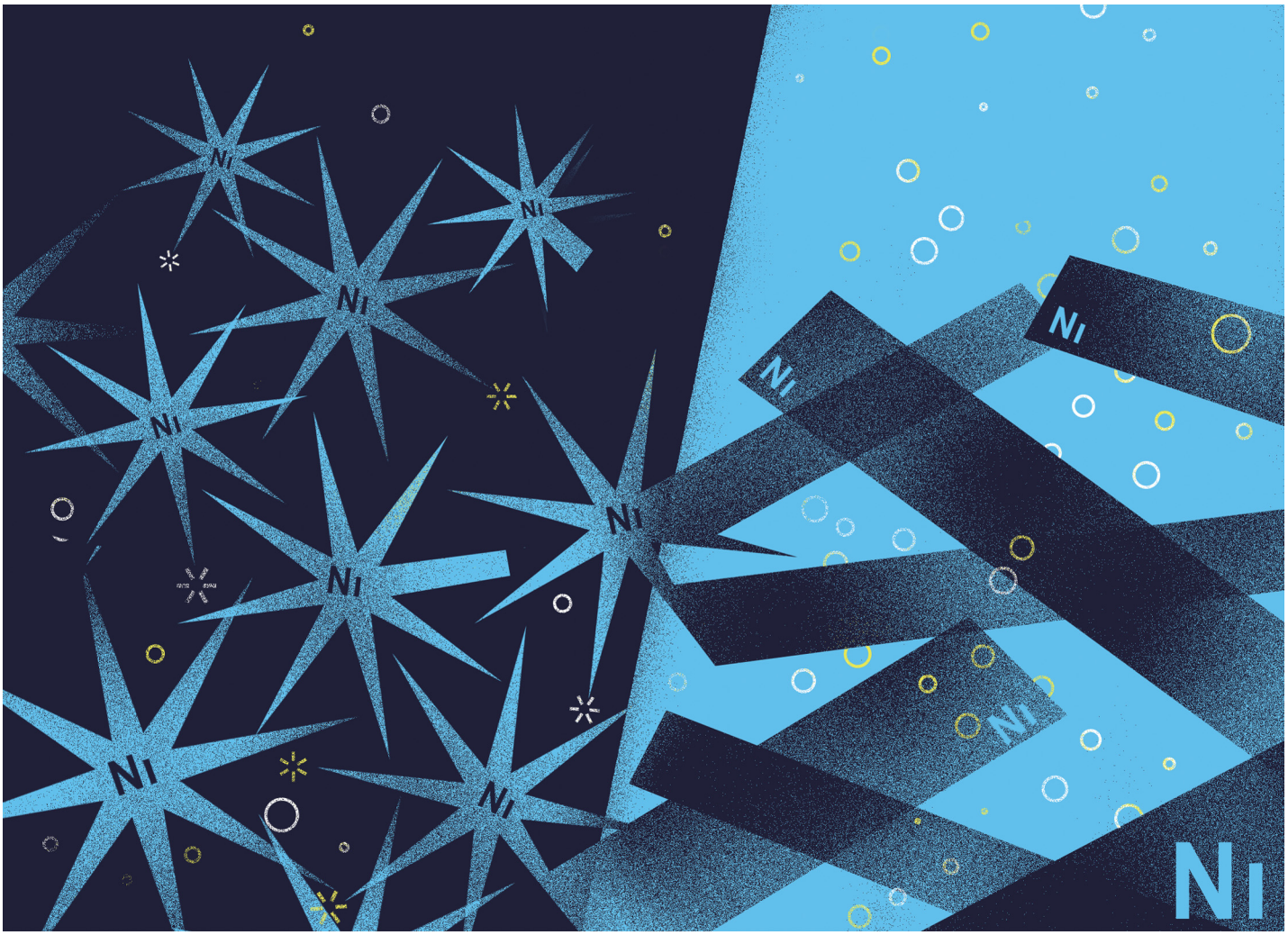

Showcasing research from Dr Pau Farras, ChemLight Laboratory, School of Biological and Chemical Sciences, Energy Research Centre, Ryan Institute, University of Galway, Ireland. Cover image designed by Catalina Parra and Agata Communications.

Hierarchical $(Ni,Co)_{0.85}Se$ sheets for efficient oxygen evolution reaction electrocatalysis: a combined approach of fabrication control and mechanistic understanding

This study reports the synthesis of hierarchical $(Ni,Co)_{0.85}Se$ sheets with enhanced oxygen evolution reaction (OER) performance. Porous architecture and Ni doping improve the OER kinetics; while DFT calculations offer insights into developing efficient, cost-effective catalysts for sustainable energy applications.

As featured in:

See Sheng Chen, Fuqiang Huang, Pau Farras *et al.*, *Chem. Commun.*, 2024, **60**, 13526.

ROYAL SOCIETY OF CHEMISTRY

rsc.li/chemcomm

Registered charity number: 207890

ChemComm

COMMUNICATION

View Article Online
View Journal | View Issue

Cite this: *Chem. Commun.*, 2024, **60**, 13526

Received 22nd August 2024,
Accepted 25th September 2024

DOI: 10.1039/d4cc04285a

rsc.li/chemcomm

Hierarchical $(Ni,Co)_{0.85}Se$ sheets for efficient oxygen evolution reaction electrocatalysis: a combined approach of fabrication control and mechanistic understanding†

Muhammad Sohail Riaz, ‡[a] Qi Huang,‡[c] Jingjing Duan, [c] Sheng Chen, *[c] Fuqiang Huang*[b] and Pau Farras *[a]

We present a fabrication process for hierarchical $(Ni,Co)_{0.85}Se$ sheets, achieving efficient oxygen evolution reaction (OER) activity with a 10 mA cm^{-2} current density at an overpotential of 290 mV. Porous architecture and doping improve kinetics, supported by DFT calculations. This approach offers insights into designing stable, high-performance OER catalysts.

Green hydrogen is considered the most environmentally friendly alternative to conventional fossil fuels as a zero-carbon fuel and energy vector.[1] However, hydrogen production is still predominantly achieved through steam reforming of natural gas. This mature technology keeps prices low in the reasonably small current hydrogen market but adds a significant carbon footprint.[2] Researchers predict that electrochemical water electrolysis powered by renewable energy sources will soon be the ideal technology for producing clean hydrogen.[3] However, reducing costs is necessary to enhance its market competitiveness. The efficiency of this process heavily depends on the performance of oxygen evolution reaction (OER) catalysts at the anode, which face challenges due to the slow four-electron transfer reaction.[4] These catalysts depend on costly noble metals, such as IrO_2 or RuO_2, significantly contributing to their overall cost.[5] Consequently, researchers worldwide are working to develop effective, earth-abundant, robust, and scalable catalysts.[6–8] Due to their low cost and abundance, efforts to replace precious metal catalysts in electrocatalysis have focused on first-row transition metals.[9–11] Our bimetallic $(Ni,Co)_{0.85}Se$ catalyst surpasses $Co_{0.85}Se$ and RuO_2 in alkaline media, owing to its unique morphology, metallic nature, and porous, layered structure that enhances charge transfer and provides easier access to active sites. DFT calculations show that Ni doping optimises electronic structure, improving OER kinetics by affecting intermediate Co-site interactions. This research underscores the value of fundamental studies for designing efficient catalysts in energy storage, conversion, and environmental applications.

We synthesized the $(Ni,Co)_{0.85}Se$ catalyst using a hydrothermal method (Fig. 1). Ni and Co nitrate salts, urea, and PVP (K30) were dissolved in distilled water, stirred, and autoclaved at 160 °C for 1 to 6 hours with Ni doping levels of 0%, 5%, 10%, and 15%. Products were extracted hourly and characterized by SEM and XRD (Fig. S1–S7, ESI†). XRD showed a transition from nanoneedle assemblies to uniform layered sheets after 6 hours (Fig. 1d and Fig. S6, ESI†). Final sheets were obtained using Na_2SeO_3 and N_2H_4 (Fig. 1e and Fig. S8, ESI†), and SEM confirmed a rough, porous surface. The morphology of

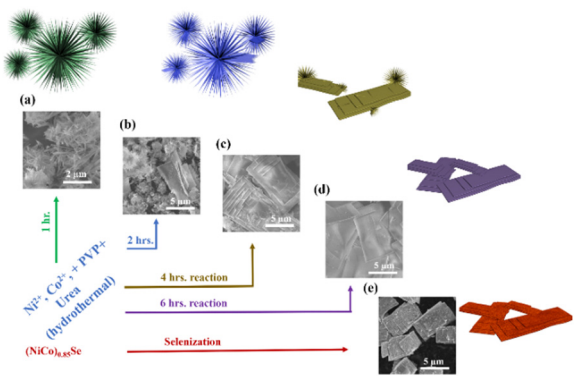

Fig. 1 (a)–(d) Synthesis scheme and corresponding SEM images of the materials from 1 to 6 hours reaction time; (e) $(Ni,Co)_{0.85}Se$ porous sheets after selenisation.

[a] *School of Biological and Chemical Sciences, Energy Research Centre, Ryan Institute, University of Galway, H91 CF50 Galway, Ireland. E-mail: pau.farras@universityofgalway.ie*

[b] *State Key Lab of Metal Matrix Composites, School of Materials Science and Engineering, Shanghai Jiao Tong University, Shanghai 200240, China. E-mail: huangfq@sjtu.edu.cn*

[c] *Key Laboratory for Soft Chemistry and Functional Materials (Ministry of Education), School of Chemical Engineering, School of Energy and Power Engineering, Nanjing University of Science and Technology, Nanjing, 210094, China. E-mail: sheng.chen@njust.edu.cn*

† Electronic supplementary information (ESI) available. See DOI: https://doi.org/10.1039/d4cc04285a

‡ These authors contributed equally to this work.

undoped $Co_{0.85}Se$ is shown for comparison (Fig. S9, ESI†). The detailed formation mechanism of micro sheets and needle-like structures is given in (ESI†).

The hexagonal crystal structure of $(Ni,Co)_{0.85}Se$ is shown in (Fig. 2a and b). X-ray diffraction (XRD) analysis confirms the phase purity of the sample, matching the hexagonal phase of $Co_{0.85}Se$ with defined diffraction peaks at $2\theta = 33.3^\circ$, 45.2°, and 51.2°, corresponding to the (101), (102), and (110) planes (JCPDS card no. 52-1108). Minor peak shifts indicate successful Ni doping without impurity phases in the Ni-doped samples compared to the undoped samples, confirming pure metallic phase formation. The XRD patterns for all Ni-doped and undoped samples are shown in (Fig. 2c), with sharp peaks indicating high crystallinity. Scanning electron microscopy (SEM) images reveal that 6h-$Ni_xCo_{2-x}(CO)_3(OH)_2$ consists of self-assembled, closely packed nanoneedles (Fig. S1, ESI†). The $(Ni,Co)_{0.85}Se$ sheets, obtained from the 6h-$Ni_xCo_{2-x}(CO)_3(OH)_2$, exhibit a rough, highly porous surface with numerous nanocrystals. These features enhance the specific surface area and facilitate rapid oxygen diffusion and mass transport, which are crucial for effective electrocatalysis. In contrast, undoped $Co_{0.85}Se$ forms a small size sheet after six hours (Fig. S9, ESI†).

Transmission electron microscopy (TEM) further characterises the morphology of $(Ni,Co)_{0.85}Se$, corroborating the SEM observations. Fig. 3a reveals that nanoparticles within the micro-sheets are interconnected, forming a well-defined layered structure without significant aggregation, as shown in (Fig. 3b). Non-uniform distribution can lead to accumulation, potentially impeding active site exposure.[12] High-resolution TEM images show lattice fringes of 0.268 nm, aligning with the (101) plane of $Co_{0.85}Se$ as indicated by XRD. Selected area electron diffraction (SAED) patterns in (Fig. 3c) display bright rings corresponding to the (101), (102), and (110) planes, confirming the crystalline nature of $(Ni,Co)_{0.85}Se$. Additionally, energy-dispersive spectroscopy (EDS) mapping in (Fig. 3e) confirms the homogeneous distribution of Ni, Co, and Se across the catalyst. TEM images for undoped $Co_{0.85}Se$ and 15% Ni-doped $Co_{0.85}Se$ are provided in (Fig. S10 and S11, ESI†) respectively.

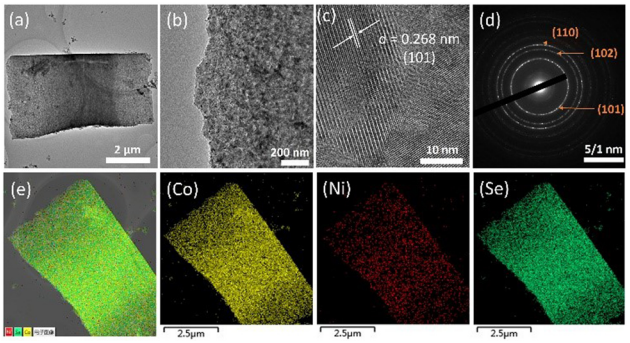

Fig. 3 Morphology characterisation of the 10% Ni-doped $(Ni,Co)_{0.85}Se$. (a) and (b) TEM images; (c) HRTEM with lattice fringes; (d) SAED selected area electron diffraction; (e) EDS elemental mapping (Co, Ni, Se).

X-ray photoelectron spectroscopy (XPS) was used to determine the valence states of the elements in the $(Ni,Co)_{0.85}Se$ micro-sheets. The XPS spectra for Ni 2p, Co $2p_{3/2}$, and Se 3d are shown in (Fig. 4). The Co $2p_{3/2}$ spectrum (Fig. 4a) shows binding energies at 781.1 eV and 778.5 eV, corresponding to Co^{3+} and Co^{2+}, respectively.[13] The Ni 2p spectrum (Fig. 4b) displays binding energies at 855.8 eV and 873.5 eV, attributed to Ni $2p_{3/2}$ and Ni $2p_{1/2}$, indicating Ni^{2+} presence.[9] The Se 3d spectrum (Fig. 4c) reveals two types of metal–selenium bonds with peaks at 53.6 eV and 54.2 eV, suggesting the formation of Ni–Se and Co–Se bonds. A peak at 60.0 eV corresponds to Se–O,[14] indicating partial contamination was removed through electrochemical preconditioning before LSV measurements in 0.1 M KOH. Also, two peaks at 58 eV and 59 eV corresponding to Co $3p_{3/2}$ can be observed, assigned to the two oxidation states as seen for Co $2p_{3/2}$.

BET (Brunauer–Emmett–Teller) analysis and N_2 sorption isotherms (Fig. 4d–f) were used to assess the specific surface area (SSA) and pore distribution of $(Ni,Co)_{0.85}Se$ sheets. The isotherms, classified as type IV with H3-type hysteresis loops, indicate mesoporous characteristics. The BET SSA values are 16.95 $m^2\ g^{-1}$ for 5% Ni-doped sheets, 18.33 $m^2\ g^{-1}$ for 10% Ni-doped, and 14.28 $m^2\ g^{-1}$ for 15% Ni-doped, with pore volumes of 0.72, 0.90, and 1.98 $cm^3\ g^{-1}$, respectively. The average pore

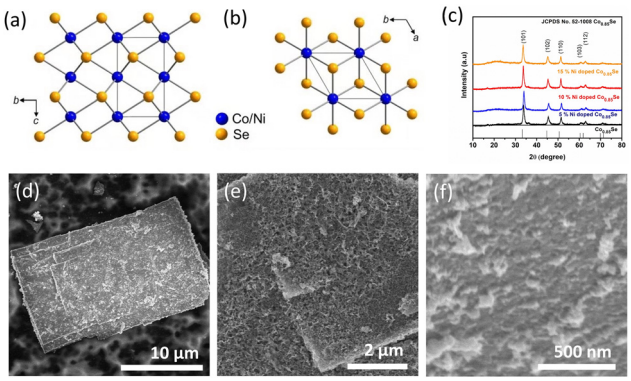

Fig. 2 Structural and morphological characterisation of as-obtained $(Ni,Co)_{0.85}Se$. (a) and (b) Crystal structures; (c) XRD patterns of $Co_{0.85}Se$ and $(Ni,Co)_{0.85}Se$ with different Ni doping; (d)–(f) representative SEM images for as-prepared $(Ni,Co)_{0.85}Se$.

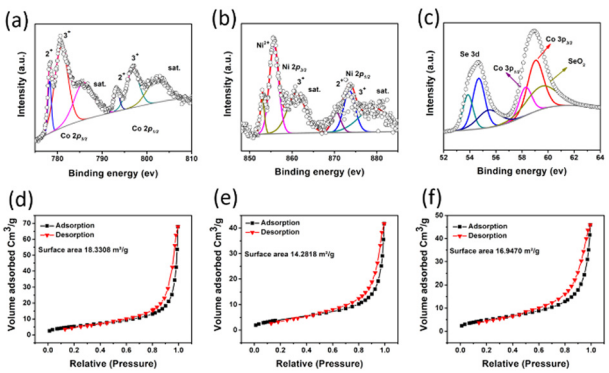

Fig. 4 X-ray photoelectron spectroscopy for (a) Co; (b) Ni; (c) Se; BET surface area for (d) 10% Ni-doped $(Ni,Co)_{0.85}Se$; (e) undoped $Co_{0.85}Se$; and (f) 15% Ni-doped $(Ni,Co)_{0.85}Se$.

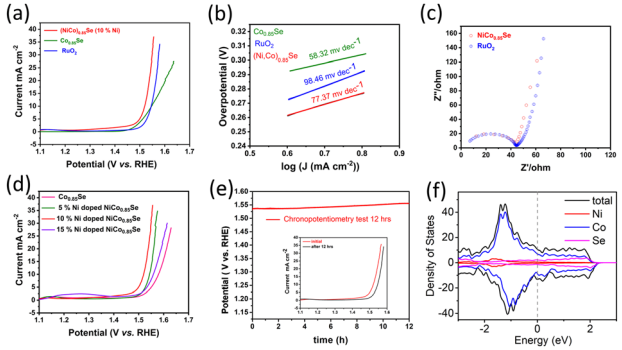

Fig. 5 (a) LSV polarization curves for OER in 0.1 M KOH after 10 activation cycles at 5 mV s^{-1} between 0.9–1.8 V *vs.* RHE; (b) Tafel slopes; (c) Nyquist plot of AC impedance; (d) polarization curves for OER with increasing Ni doping concentrations; (e) chronopotentiometry test (inset: comparison before and after OER); (f) DOS calculation for $(Ni,Co)_{0.85}Se$.

diameter, determined *via* the BJH method (Fig. S12, ESI†), is 1.77 nm. As Ni content increases, higher nucleation rates lead to smaller particles and more significant surface areas (*e.g.* 18.33 m^2 g^{-1} for 10% Ni-doped). However, excess Ni (15% Ni-doped) causes particle aggregation, reducing the surface area (14.28 m^2 g^{-1}).

We investigated the OER performance of catalysts in a 0.1 M KOH solution using electrocatalyst-coated glassy carbon electrodes. The catalysts were electrochemically conditioned with cyclic voltammetry (CV) before evaluating water oxidation *via* linear sweep voltammetry (LSV). As shown in Fig. 5a, the IR-corrected LSV polarization curves, recorded at a 5 mV s^{-1} scan rate, reveal that both $(Ni,Co)_{0.85}Se$ and $Co_{0.85}Se$ demonstrate high OER activity with clear oxidation features. The performance comparison of the catalyst with those of the reported catalysts is given in (Table S1, ESI†). The anodic peak rise during water oxidation suggests Ni doping created additional active sites.

Electrochemical impedance spectroscopy (EIS) showed that $(Ni,Co)_{0.85}Se$ has lower charge transfer resistance than commercial RuO_2, due to its complete electrode assembly and Ni integration into the $Co_{0.85}Se$ lattice.[15] This lower resistance enhances electron transport at the electrolyte/electrode interface and within the electrode bulk, minimising *iR* losses.[16] The equivalent circuit of EIS spectra and corresponding fitting data are given in (Fig. S13, ESI†). The hydrophilic nature of the $(Ni,Co)_{0.85}Se$ sheets ensures complete wetting of the selenide surfaces due to its porous structure,[17] which improves electrolyte ion trapping and access to active sites. This hydrophilicity suggests surface hydroxylation, likely due to oxyhydroxide formation or the substitution of surface oxygen atoms with hydroxyl groups. Key metrics for evaluating OER performance include the overpotential at a current density of 10 mA cm^{-2}, $(Ni,Co)_{0.85}Se$ achieves an overpotential of 290 mV at 10 mA cm^{-2}, compared to 320 mV for $Co_{0.85}Se$ and RuO_2. At 25 mA cm^{-2}, $(Ni,Co)_{0.85}Se$ achieves an overpotential of 310 mV, outperforming RuO_2 (340 mV) and $Co_{0.85}Se$ (390 mV). Its Tafel slope is 77.37 mV dec^{-1}, lower than RuO_2's 98.46 mV dec^{-1}, reflecting better OER kinetics. Among Ni doping levels (5%, 10%, 15%), 10% doping yields the best performance. Impedance spectroscopy shows a charge transfer resistance of 0.45 Ω (Fig. 5c). The electrode remains stable during a 12-hour chronopotentiometry test at 10 mA cm^{-2}, with minimal potential fluctuation and effective O_2 bubble removal. Theoretical analysis (Fig. 5f) indicates a high and stable density of states (DOS) near the Fermi level, which enhances its electrical properties and performance. Post-catalytic analysis following a 12-hour chronopotentiometry test (as shown in transmission electron microscopy in (Fig. S14, ESI†) reveals that $(Ni,Co)_{0.85}Se$ transforms into nickel cobalt oxyhydroxides during the oxygen evolution reaction (OER)). This demonstrates that metal oxyhydroxides are the active and final forms of metal selenide pre-catalysts in OER. These findings confirm that metal selenides serve as templating precursors for forming highly active metal oxyhydroxide OER catalysts.

Spin-polarised density functional theory (DFT) calculations were used to investigate OER catalysis by creating a model of $Co_{35}Ni_4Se_{46}$, where 10% of Co atoms were replaced with Ni. This model was sliced along the (101) crystal plane to study the adsorption and desorption of OER intermediates, including *OH, *O, *OOH, and *O_2. Geometry optimisations for these intermediates (Fig. S15, ESI†) allowed the calculation of Gibbs free energies (see Computational methods). As shown in Fig. 6a, the intermediates adsorbed on Co active sites of $(Ni,Co)_{0.85}Se$ exhibited several uphill reaction steps at 0 V where the most endothermic step is considered as the rate-determining step (RDS).[18] The corresponding Gibbs free energy change (ΔG) of RDS is a critical criterion for evaluating OER catalytic activities as the conversion of *OOH from *O for $(Ni,Co)_{0.85}Se$, requiring a minimum potential of 1.41 V (or an overpotential of 0.18 V), enabling OER to occur (Fig. 6a).[19,20] These results are consistent with previous examples in the literature where *OOH is usually the RDS because of its weak

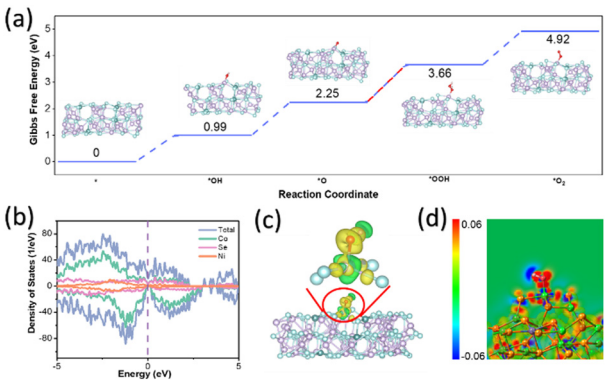

Fig. 6 (a) Gibbs free energy change of OER on $(Ni,Co)_{0.85}Se$; (b) theoretical DOS; (c) side view of charge density difference for OH adsorption on $(Ni,Co)_{0.85}Se$, with charge accumulation (yellow) and depletion (green). Inset shows the most stable configuration. Colour code: Co (purple), Ni (green), Se (reseda), O (red), H (pink); (d) 2D sectional view of charge density difference for adsorbed OH on $(Ni,Co)_{0.85}Se$, with charge accumulation (red) and depletion (blue). These results highlight $(Ni,Co)_{0.85}Se$'s high catalytic activity with *O to *OOH as the RDS for alkaline OER, aiding in electrocatalyst optimization for sustainable energy applications.

bonding to the surface as compared to other molecules in alkaline medium.[21] The mechanism for the RDS was studied using a density of states (DOS) and charge density difference. Fig. 6b shows that the DOS profile of $(Ni,Co)_{0.85}Se$ spans the Fermi level without a bandgap in spin-up or spin-down channels, indicating metallic properties and excellent electronic conductivity for charge transfer during OER. This aligns well with the calculated DOS of *OH, *O, and *OOH (Fig. S16, ESI†), showing moderate interaction of these intermediates at the active site, leading to good reaction kinetics.[22] A wider pseudogap observed for the *OOH intermediate than *O indicates a stronger bond interaction, making *OOH the RDS for OER. Charge density difference mappings for *OH (Fig. 6c), *O, and *OOH (Fig. S17, ESI†) provide further evidence for the RDS.[23]

The apparent charge transfer between Co and O atoms has been observed, indicating the formation of Co–O bonds inside these OER intermediates.[24,25] Notably, the 2D sectional view of charge density difference (Fig. 6d and Fig. S18, ESI†) reveals more red area for *O than *OOH and others, thus confirming the difficulty of transforming from *O to *OOH.

In conclusion, metallic $(Ni,Co)_{0.85}Se$ porous sheets demonstrate superior performance as OER electrocatalysts compared to previous 3d-metal-based alternatives. Our study highlights that Ni doping enhances the OER activity of $Co_{0.85}Se$, making $(Ni,Co)_{0.85}Se$ an effective and selective support for other OER catalysts through synergistic effects. The cost-effective, scalable synthesis supports our design strategy, offering a novel approach to high-performance OER catalysts, particularly heterostructures. This work advances the understanding of electrocatalyst structure–activity relationships, contributing to developing efficient catalysts for sustainable energy.

This study was supported by the Science and Technology Commission of Shanghai Municipality (23DZ1200800). M. S. R. and P. F. acknowledge the ANEMEL project (Grant Agreement No. 101071111) funded by the European Innovation Council.

Data availability

The data supporting the findings of this study are available within the article and its ESI.† Raw data will be made available in the ANEMEL project Zenodo account **https://zenodo.org/communities/anemel/**. The optimized atomic positions of the reaction intermediates and transition states are available from the corresponding authors on reasonable request.

Conflicts of interest

There are no conflicts to declare.

Notes and references

1 A. Odenweller, F. Ueckerdt, G. F. Nemet, M. Jensterle and G. Luderer, *Nat. Energy*, 2022, **7**, 854–865.
2 R. Kumar, R. Singh and S. Dutta, *Energy Fuels*, 2024, **38**, 2601–2629.
3 W. Tong, M. Förster, F. Dionigi, S. Dresp, R. S. Erami, P. Strasser, A. J. Cowan and P. Farràs, *Nat. Energy*, 2021, **6**, 935.
4 N. Han, W. Zhang, W. Guo, H. Pan, B. Jiang, L. Xing, H. Tian, G. Wang, X. Zhang and J. Fransaer, *Nano-Micro Lett.*, 2023, **15**, 185.
5 N. T. T. Thao, J. U. Jang, A. K. Nayak and H. Han, *Small Sci.*, 2024, **4**, 2300109.
6 K. M. P. Wheelhouse, R. L. Webster and G. L. Beutner, *Org. Process Res. Dev.*, 2023, **27**, 1157–1159.
7 J. Xu, J. Ruan, Y. Jian, J. Lao, Z. Li, F. Xie, Y. Jin, X. Yu, M. H. Lee and Z. Wang, *Small*, 2024, **20**, 2305905.
8 L. Mu, S. Qiu, G. Zhao, W. Liao, N. Zhao and X. Xu, *J. Mater. Chem. A*, 2024, **12**, 1714–1724.
9 S. Sanati, A. Morsali and H. Garcia, *Energy Environ. Sci.*, 2022, **15**, 3119–3151.
10 Y. Tong, Q. Sun, P. Chen, L. Chen, Z. Fei and P. J. Dyson, *ChemSusChem*, 2020, **13**, 5112–5118.
11 Y. Tong, H. Mao, P. Chen, Q. Sun, F. Yan and F. Xi, *Chem. Commun.*, 2020, **56**, 4196–4199.
12 W. Chen, L. Zhang, L. Xu, Y. He, H. Pang, S. Wang and Y. Zou, *Nat. Commun.*, 2024, **15**, 2420.
13 Y. Chen, L. Wang, H. Gan, Y. Jiang, J. Feng, J. Liu and X. Shi, *J. Energy Storage*, 2022, **47**, 103625.
14 U. Weser, G. Sokolowski and W. Pilz, *J. Electron Spectrosc. Relat. Phenom.*, 1977, **10**, 429–439.
15 J. A. Rajesh, J. Y. Kim, S. H. Kang and K. S. Ahn, *Micromachines*, 2023, **14**, 1905.
16 X. Leng, L. Zhao, W. Shi, J. Lian and X. Zhang, *J. Phys. Chem. C*, 2024, **128**, 9422–9434.
17 C. Xia, Q. Jiang, C. Zhao, M. N. Hedhili and H. N. Alshareef, *Adv. Mater.*, 2015, **28**, 77–85.
18 J. Yang, Y. Wang, J. Yang, Y. Pang, X. Zhu, Y. Lu, Y. Wu, J. Wang, H. Chen, Z. Kou, Z. Shen, Z. Pan and J. Wang, *Small*, 2022, **18**, 2106187.
19 J. Gu, S. Magagula, J. Zhao and Z. Chen, *Small Methods*, 2019, **3**, 1800550.
20 Y. Zhao, P. Zhang, Z. Yang, L. Li, J. Gao, S. Chen, T. Xie, C. Diao, S. Xi, B. Xiao, C. Hu and W. Choi, *Nat. Commun.*, 2021, **12**, 3701.
21 W. Xu, N. Apodaca, H. Wang, L. Yan, G. Chen, M. Zhou, D. Ding, P. Choudhury and H. Luo, *ACS Catal.*, 2019, **9**, 5074–5083.
22 Y. Sun, B. Xia, S. Ding, L. Yu, S. Chen and J. Duan, *J. Mater. Chem. A*, 2021, **9**, 20040–20047.
23 D. Chen, Y. Wang, D. Liu, H. Liu, C. Qian, H. He and J. Yang, *Carbon Energy*, 2020, **2**, 443–451.
24 S. Wang, K. Uwakwe, L. Yu, J. Ye, Y. Zhu, J. Hu, R. Chen, Z. Zhang, Z. Zhou, J. Li, Z. Xie and D. Deng, *Nat. Commun.*, 2021, **12**, 7072.
25 Y. Sun, S. Ding, B. Xia, J. Duan, M. Antonietti and S. Chen, *Angew. Chem., Int. Ed.*, 2022, **61**, e202115198.